Check for updates

RESEARCH ARTICLES

SUPERCONDUCTIVITY

Pair wave function symmetry in UTe_2 from zero-energy surface state visualization

Qiangqiang Gu[1]*†, Shuqiu Wang[1,2,3]†, Joseph P. Carroll[1,4]†, Kuanysh Zhussupbekov[1,4]†, Christopher Broyles[5], Sheng Ran[5], Nicholas P. Butch[6,7], Jarryd A. Horn[6], Shanta Saha[6], Johnpierre Paglione[6,8], Xiaolong Liu[1,9,10], J. C. Séamus Davis[1,2,4,11]*, Dung-Hai Lee[12,13]*

Although nodal spin-triplet topological superconductivity appears probable in uranium ditelluride (UTe_2), its superconductive order parameter $\Delta_{\mathbf{k}}$ remains unestablished. In theory, a distinctive identifier would be the existence of a superconductive topological surface band, which could facilitate zero-energy Andreev tunneling to an s-wave superconductor and also distinguish a chiral from a nonchiral $\Delta_{\mathbf{k}}$ through enhanced s-wave proximity. In this study, we used s-wave superconductive scan tips and detected intense zero-energy Andreev conductance at the UTe_2 (0-11) termination surface. Imaging revealed subgap quasiparticle scattering interference signatures with *a*-axis orientation. The observed zero-energy Andreev peak splitting with enhanced s-wave proximity signifies that $\Delta_{\mathbf{k}}$ of UTe_2 is a nonchiral state: B_{1u}, B_{2u}, or B_{3u}. However, if the quasiparticle scattering along the *a* axis is internodal, then a nonchiral B_{3u} state is the most consistent for UTe_2.

The internal symmetry of electron-pair wave functions in nontrivial superconductors (*1*) is represented by the momentum $\mathbf{p} = \hbar\mathbf{k}$ dependence of the electron-pairing order parameter $\Delta_{\mathbf{k}}$, where $\hbar$ is the reduced Planck constant. For spin-triplet superconductors, where electron pairs have three spin-1 eigenstates ($|\uparrow\uparrow\rangle, |\downarrow\downarrow\rangle, |\uparrow\downarrow + \downarrow\uparrow\rangle$), $\Delta_{\mathbf{k}}$ is a 2×2 matrix: $\Delta_{\mathbf{k}} = \begin{pmatrix} \Delta_{\mathbf{k}\uparrow\uparrow} & \Delta_{\mathbf{k}\uparrow\downarrow} \\ \Delta_{\mathbf{k}\downarrow\uparrow} & \Delta_{\mathbf{k}\downarrow\downarrow} \end{pmatrix}$ with $\Delta^{\mathrm{T}}_{-\mathbf{k}} = -\Delta_{\mathbf{k}}$ and $\Delta_{\mathbf{k}} = \Delta^{\mathrm{T}}_{\mathbf{k}}$ (*1–5*). This may also be represented in the **d**-vector notation as $\Delta_{\mathbf{k}} \equiv \Delta_0(\mathbf{d}\cdot\boldsymbol{\sigma})i\sigma_2$ where σ_i are the Pauli matrices. Many such systems should be intrinsic topological superconductors (ITSs), where a bulk superconducting energy gap with nontrivial topology coexists with a symmetry-protected topological surface band (TSB) of Bogoliubov quasiparticles within that energy gap. Unlike proximitized topological insulators or semiconductors, when three-dimensional (3D) superconductors are topological (*6*), it is not because of electronic band structure topology but rather because $\Delta_{\mathbf{k}}$ exhibits topologically nontrivial properties (*7*). The prototypical example would be a 3D spin-triplet nodal superconductor (*1–6*), and the search for such ITSs that are also technologically viable is a forefront of quantum matter research (*8*).

Three-dimensional spin-triplet superconductors are complex states of quantum matter (*1*, *4*, *5*). Thus, for pedagogical purposes, we describe a nodal spin-triplet superconductor using a spherical Fermi surface within a cubic 3D Brillouin zone (Fig. 1A). The zeros of $\Delta_{\mathbf{k}}$ are then represented by red points at $\pm\mathbf{k}_n$. The Bogoliubov–de Gennes (BdG) Hamiltonian is given by

$$H = \sum_{k_x}\sum_{\mathbf{k}_\perp} \psi^+(k_x, \mathbf{k}_\perp) h(k_x, \mathbf{k}_\perp) \psi(k_x, \mathbf{k}_\perp) \quad (1)$$

Here $\psi^T(\mathbf{k}) = \left(c_{\mathbf{k}\uparrow}, c_{\mathbf{k}\downarrow}, c^+_{-\mathbf{k}\uparrow}, c^+_{-\mathbf{k}\downarrow}\right)$ and $h(k_x, \mathbf{k}_\perp)$ is a 4×4 matrix, containing both band structure and $\Delta_{\mathbf{k}}$. We distinguish $\mathbf{k} = (k_x, \mathbf{k}_\perp)$ because they play different roles in the following didactic presentation. Considering one particular 2D slice of the 3D Brillouin zone with a fixed k_x: Its Hamiltonian $h(k_x, \mathbf{k}_\perp)$ is that of a 2D superconductor within a 2D Brillouin zone spanned by $\mathbf{k}_\perp$. The 2D states $|k_x| < |\mathbf{k}_n|$ (Fig. 1A, blue) are topological and those $|k_x| > |\mathbf{k}_n|$ (Fig. 1A, green) are nontopological. The essential signature of such physics is a superconductive TSB [or Andreev bound state (ABS) (*7*)] on the edges of each 2D slice for $|k_x| < |\mathbf{k}_n|$, and its absence when $|k_x| > |\mathbf{k}_n|$. The 2D Brillouin zone of any crystal surface parallel to the nodal axis of $\Delta_{\mathbf{k}}$ is shown in Fig. 1B along with the quasiparticle dispersion $\mathbf{k}(E)$ of a single TSB. The equatorial circle in Fig. 1B is the $k_x - k_y$ contour satisfying $\epsilon(k_x, k_y, 0) = 0$ with $\epsilon(k)$ being the quasiparticle band dispersion. A line of zero-energy TSB states then connects the two projections of the nodal wave vectors $\pm\mathbf{k}_n$ onto this 2D zone (this is often called a "Fermi arc," although it is actually a twofold degenerate Majorana arc of charge-neutral Bogoliubov quasiparticles). Calculation of the density of such TSB quasiparticle states $N(E)$ from $\mathbf{k}(E)$ in Fig. 1B yields a continuum in the range $-\Delta_0 \le E \le \Delta_0$, with a sharp central peak at $E = 0$ due to this arc (Fig. 1C). Thus, 3D nodal spin-triplet superconductors should exhibit a TSB on any surface parallel to their nodal axis, and such TSBs exhibit a zero-energy peak in $N(E)$ [see supplementary text section 1 of (*9*)]. The conceptual phenomena presented in Fig. 1, A to C, depend solely on whether the symmetry protecting the TSB is broken, and not on material details. Hence, the presence or absence of a gapless TSB on a given surface of a 3D superconductor, of a zero-energy peak in $N(E)$ from its Majorana arcs, and of the response of the TSB to breaking specific symmetries can reveal the symmetry and topology of $\Delta_{\mathbf{k}}$.

Pair wave function symmetry in UTe_2

UTe_2 is now the leading candidate 3D nodal spin-triplet superconductor (*10*, *11*). Its crystal symmetry point group is D_{2h} and the space group is *Immm* [section 2 of (*9*)]. Associated with the three basis vectors **a**, **b**, and **c** are the three orthogonal **k**-space axes k_x, k_y, k_z. Within D_{2h} there are four possible odd-parity order parameter symmetries designated A_u, B_{1u}, B_{2u}, and B_{3u} [section 2 of (*9*)]. All preserve time-reversal symmetry: A_u is fully gapped, whereas B_{1u}, B_{2u}, and B_{3u} have zeros (point nodes) in $\Delta_{\mathbf{k}}$, whose axial alignment is along **c**, **b**, or **a**, respectively [section 2 of (*9*)]. Linear combinations of A_u, B_{1u}, B_{2u}, and B_{3u} are also possible, which break point-group and time-reversal symmetries, resulting in a chiral TSB (*7*, *8*). For UTe_2, there are two chiral states of particular interest with $\Delta_{\mathbf{k}}$ nodes aligned with the crystal *c* axis, and two with nodes aligned with the *a* axis [section 2 of (*9*)]. Although identifying which (if any) of these superconductive states exists in UTe_2 is key to its fundamental physics, this objective has proven extraordinarily difficult to achieve (*12*).

Identifying the $\Delta_{\mathbf{k}}$ symmetry of UTe_2 using macroscopic experiments has been problematic because, depending on the sample preparation method, the UTe_2 samples appear to have various degrees of heterogeneity. Samples grown by chemical vapor transport (CVT) exhibit small residual resistivity ratios (RRRs) (~*35*) and transition temperatures $T_c \approx$ 1.6 to 2 K (*13–15*), whereas samples grown by the molten flux method (MFM) have larger RRRs (~1000) and higher transition temperatures ($T_c \approx 2$ K) (*16*). From macroscopic studies, the status $\Delta_{\mathbf{k}}$ for UTe_2 remains indeterminate (*17–27*) [section 3 of (*9*)]. To date, $\Delta_{\mathbf{k}}$ symmetry of UTe_2

[1]Lab of Atomic and Solid State Physics (LASSP), Department of Physics, Cornell University, Ithaca, NY, USA. [2]Clarendon Laboratory, University of Oxford, Oxford, UK. [3]H. H. Wills Physics Laboratory, University of Bristol, Bristol, UK. [4]Department of Physics, University College Cork, Cork, Ireland. [5]Department of Physics, Washington University in St. Louis, St. Louis, MO, USA. [6]Maryland Quantum Materials Center, University of Maryland, College Park, MD, USA. [7]NIST Center for Neutron Research, Gaithersburg, MD, USA. [8]Canadian Institute for Advanced Research, Toronto, Ontario, Canada. [9]Department of Physics and Astronomy, University of Notre Dame, Notre Dame, IN, USA. [10]Stavropoulos Center for Complex Quantum Matter, University of Notre Dame, Notre Dame, IN, USA. [11]Max-Planck Institute for Chemical Physics of Solids, Dresden, Germany. [12]Department of Physics, University of California, Berkeley, Berkeley, CA, USA. [13]Materials Sciences Division, Lawrence Berkeley National Laboratory, Berkeley, CA, USA. ***Corresponding author. Email: qiangqianggu2016@gmail.com (Q.G.); jcseamusdavis@gmail.com (J.C.S.D.); dunghai@berkeley.edu (D.-H.L.)** †These authors contributed equally to this work.

Downloaded from https://www.science.org at University of Maryland College Park on June 16, 2025

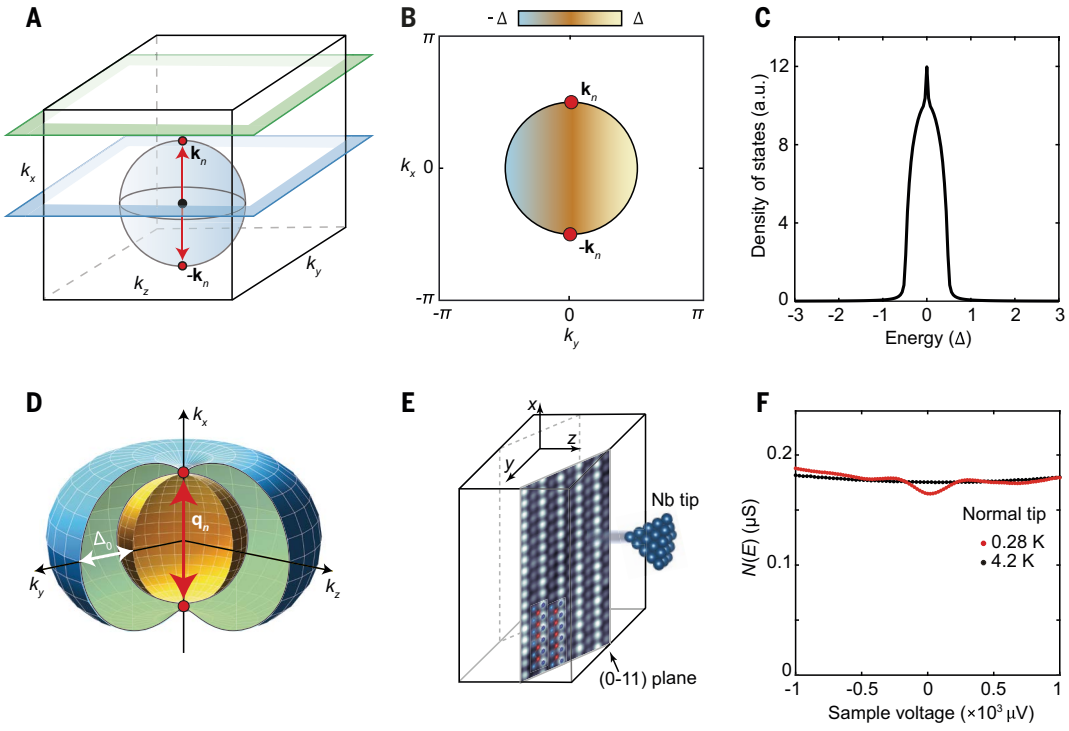

Fig. 1. Pair wave function symmetry in UTe_2. (**A**) Pedagogical model of a nodal spin-triplet superconductor with order parameter $\Delta_{\mathbf{k}}$ having *a*-axis nodes identified by red dots; the red arrow labels the internodal scattering wave vector. The 2D states $|k_x| < |\mathbf{k}_n|$ indicated for example by a blue plane are topological, whereas those $|k_x| > |\mathbf{k}_n|$, indicated by a green plane, are nontopological. (**B**) The 2D Brillouin zone of the crystal surface parallel to the $\Delta_{\mathbf{k}}$ nodal axis, namely, the *a*-*b* plane, showing a single TSB dispersion $\mathbf{k}(E)$ with color code for *E*. A line of zero-energy TSB states dubbed the Fermi arc connects the two points representing the projections of the 3D $\Delta_{\mathbf{k}}$ nodal wave vectors $\pm\mathbf{k}_n(E)$ onto this 2D zone. The equatorial circle in this plot is the $k_x - k_y$ contour satisfying $\epsilon(k_x,k_y,0) = 0$ where $\epsilon(k_x,k_y,k_z)$ is the band dispersion used in the model. (**C**) The density of TSB quasiparticle states $N(E)$ calculated from (B) exhibits a continuum $|E| \leq \Delta_0$ with a sharp peak at $E = 0$ owing to the TSB Fermi arc. a.u., arbitrary units. (**D**) Schematic symmetry of a possible UTe_2 order parameter $\Delta_{\mathbf{k}}$ that has two *a*-axis nodes. The *a* axis–oriented internodal scattering $\mathbf{q}_n$ is indicated by a red arrow. (**E**) Schematic of (0-11) cleave surface of UTe_2 shown in relative orientation to the STM tip tunneling direction and $\Delta_{\mathbf{k}}$ in (D). (**F**) Measured $N(E)$ of normal ($T = 4.2$ K) and superconducting ($T = 280$ mK) states of UTe_2 using a nonsuperconducting STM tip at the (0-11) cleave surface as seen in (E). At the UTe_2 surface, virtually all states $|E| \leq \Delta_0$ are ungapped.

has been conjectured as nonchiral A_u (*17*, *20*), B_{1u} (*24*), B_{3u} (*18*, *24*), chiral $A_u + iB_{3u}$ (*21*), $B_{2u} + iB_{3u}$ (*22*), $A_u + iB_{1u}$ (*22*), and $B_{1u} + iB_{2u}$ (*26*). Notably, however, no tunneling spectroscopic measurements of $\Delta_{\mathbf{k}}$, which could differentiate directly between these scenarios, have been reported.

Tunneling between s-wave and topological p-wave superconductors

An efficient tunneling spectroscopic technique for establishing $\Delta_{\mathbf{k}}$ in unconventional superconductors (*28*–*33*) is quasiparticle interference imaging (QPI); but this has proven ineffective for unraveling the conundra of UTe_2. This is because conventional single-electron tunneling spectroscopy of UTe_2, even at $T = 280$ mK ($T/T_c \lesssim 1/6$), yields a typical quasiparticle density-of-states spectrum $N(E \leq \Delta_0)$ that is essentially metallic, with only tenuous hints of opening the bulk superconductive energy gap (Fig. 1F) (*34*, *35*). Further, UTe_2 surface impedance measurements detect a nonsuperconductive component of surface conductivity $\sigma_1(\omega,T)$ deep in the superconductive phase (*36*). Yet the classic QPI signature (*37*) of a bulk superconductive $\Delta_{\mathbf{k}}$ has been impossible to detect, apparently because the high $N(E \leq \Delta_0)$ overwhelms any tunneling conductance signal from the 3D quasiparticles. Given these challenges to determining the symmetry of $\Delta_{\mathbf{k}}$ using a normal scan tip, we explored the possibility of using a superconductive scan tip [(*38*–*43*) and section 4 of (*9*)]. Theoretically, we consider two primary channels for conduction from the fully gapped s-wave superconductive tip to a nodal spin-triplet superconductor. The first is single-electron tunneling, for which the minimum voltage required is $V = \Delta_{tip}/e$. The second, is Andreev reflection of pairs of subgap quasiparticles [section 4 of (*9*)] transferring charge $2e$ across the junction: This occurs because creating or annihilating Cooper pairs costs no energy in a superconductor. Conceptually, therefore, there are notable advantages to using scanned Andreev tunneling spectroscopy for ITS studies, including that TSB quasiparticles within the interface predominate the Andreev process, that the order parameter symmetry difference between sample and tip does not preclude the resulting zero-bias Andreev conductance, and that the enhanced zero-energy conductance peak due to the TSB can be detected simply and directly in this way.

To explore this opportunity, we have developed a general guiding theoretical model to describe an s-wave superconducting tip [e.g., niobium (Nb)] connected by tunneling to a nodal p-wave superconductor (e.g., UTe_2), which sustains a TSB within the interface. We refer to this throughout as the SIP model. To simplify computational complexity, we consider a planar interface shown schematically in Fig. 2A with in-plane momenta as good quantum numbers. The BdG Hamiltonian of this SIP model has three elements: $H = H_{Nb} + H_{UTe_2} + H_T$. Here, H_{Nb} is the Hamiltonian for an ordinary s-wave superconductor given by $H_{Nb}(\mathbf{k}) = \begin{pmatrix} \epsilon_{Nb}(\mathbf{k})\sigma_0 & \Delta_{Nb}(i\sigma_2) \\ \Delta^*_{Nb}(-i\sigma_2) & -\epsilon_{Nb}(-\mathbf{k})\sigma_0 \end{pmatrix}$; $\epsilon_{Nb}(\mathbf{k})$ is the band structure model for Nb, and Δ_{Nb} is the Nb superconducting order parameter. H_{UTe_2} is the Hamiltonian of the putative p-wave superconductor with $\begin{pmatrix} \epsilon_{UTe_2}(\mathbf{k})\sigma_0 & \Delta_{UTe_2}(\mathbf{k}) \\ \Delta^+_{UTe_2}(\mathbf{k}) & -\epsilon_{UTe_2}(-\mathbf{k})\sigma_0 \end{pmatrix}$; $\epsilon_{UTe_2}(\mathbf{k})$ is the band structure, and $\Delta_{UTe_2}(\mathbf{k})$ is a 2×2 spin-triplet pairing matrix given by $\Delta_{UTe_2}(\mathbf{k}) \equiv \Delta_{UTe_2} i(\mathbf{d}\cdot\boldsymbol{\sigma})\sigma_2$. H_T is the tunneling Hamiltonian between the

Downloaded from https://www.science.org at University of Maryland College Park on June 16, 2025

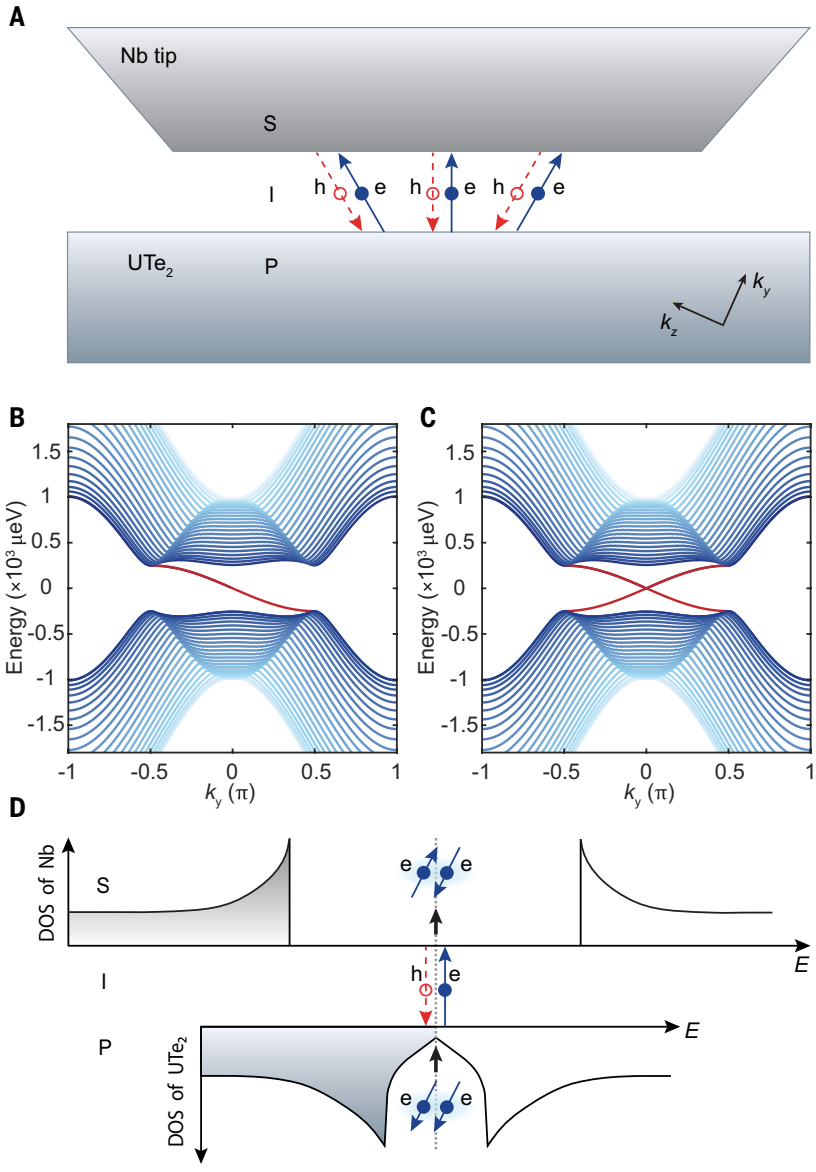

Fig. 2. SIP model: Interfacial quasiparticle TSB between p-wave and s-wave electrodes. (**A**) Schematic SIP model for interface between an s-wave electrode ("S") and a p-wave superconductor ("P") separated by an interface ("I"), containing the TSB on the surface of the p-wave superconductor. There is a variable tunneling matrix element $|M|$ between them, where $|M| \sim 1/R$ and R is the junction resistance. This model is designed to characterize a tunnel junction between superconductive Nb (S) scan tip and UTe_2 surface (P). Any superconductive TSB quasiparticles existing within the interface undergo Andreev scattering between s-wave and p-wave electrodes. (**B**) Calculated quasiparticle bands within the SIP interface for a chiral, time-reversal symmetry–breaking, p-wave order parameter with $A_u + iB_{3u}$ symmetry (table S2). The Nb electrode has trivial s-wave symmetry. For this plot, k_x is set to zero. Throughout all the calculated band dispersions, the red dispersion lines denote the superconductive TSB. The shading of the blue dispersion lines is used to highlight the low-energy band structure phenomena, which are central to the tunneling process within the SIP interface. (**C**) Calculated quasiparticle bands within the SIP interface for a nonchiral, time-reversal symmetry–conserving, p-wave order parameter with B_{3u} symmetry (table S1). Here the gapless TSB is protected by time-reversal symmetry. The value of k_x in this plot is set to zero. (**D**) Schematic of the zero-energy differential Andreev tunneling conductance $a(V) \equiv dI/dV|_{SIP}$ to the s-wave electrode. The magnitude of this zero-bias peak in $a(V)$ is determined by the density $N(0)$ of TSB quasiparticle states within the SIP interface, through a two-quasiparticle Andreev scattering process as shown. DOS, density of states.

two superconductors $H_T = -|M| \sum_{\mathbf{k}_\parallel} \left[\psi^*_{\mathrm{Nb},\mathbf{k}_\parallel} \sigma_3 \otimes \sigma_0 \psi_{\mathrm{UTe_2},\mathbf{k}_\parallel}(\mathbf{k}) + \mathrm{h.c.} \right]$.

Further, $\mathbf{k}_\parallel$ is the momentum in the plane parallel to the interface, ψ is the four-component fermion field (eq. S2) localizing on the adjacent planes of the s-wave and p-wave superconductors, and $|M|$ is the tunneling matrix element. To simplify the SIP calculation, $\epsilon_{\mathrm{Nb}}(\mathbf{k})$ and $\epsilon_{\mathrm{UTe_2}}(\mathbf{k})$ are approximated as single bands [section 4 of (*9*)], yet this alters neither the fundamental characteristics of the TSB nor the symmetry properties of the problem, both of which are controlled primarily by the symmetry and topology of $\Delta_{\mathbf{k}}$ [section 4 of (*9*)]. Finally, our simple band structure model $\epsilon_{\mathrm{UTe_2}}(\mathbf{k})$ represents a closed 3D Fermi surface [section 11 of (*9*)] upon which depends the nontrivial topology of $\Delta_{\mathbf{k}}$.

For $H_{\mathrm{UTe_2}}$, we consider two scenarios: (i) chiral pairing state $A_u + iB_{3u}$ with $\mathbf{d}(\mathbf{k}) = (0, k_y + ik_z, ik_y + k_z)$ and (ii) nonchiral pairing state B_{3u} with $\mathbf{d}(\mathbf{k}) = (0, k_z, k_y)$. In both examples, the two nodes of $\Delta_{\mathbf{k}}$ lie along the a axis, as in Fig. 1A, and we use $\Delta_{\mathrm{UTe_2}} = \frac{1}{5}\Delta_{\mathrm{Nb}}$. First, for $|M| = 0$, we solve the spectrum of $H_{\mathrm{UTe_2}}$ exactly. Figure 2B shows the quasiparticle eigenstates $E(k_x = 0, k_y)$ plotted versus k_y for the chiral order

Downloaded from https://www.science.org at University of Maryland College Park on June 16, 2025

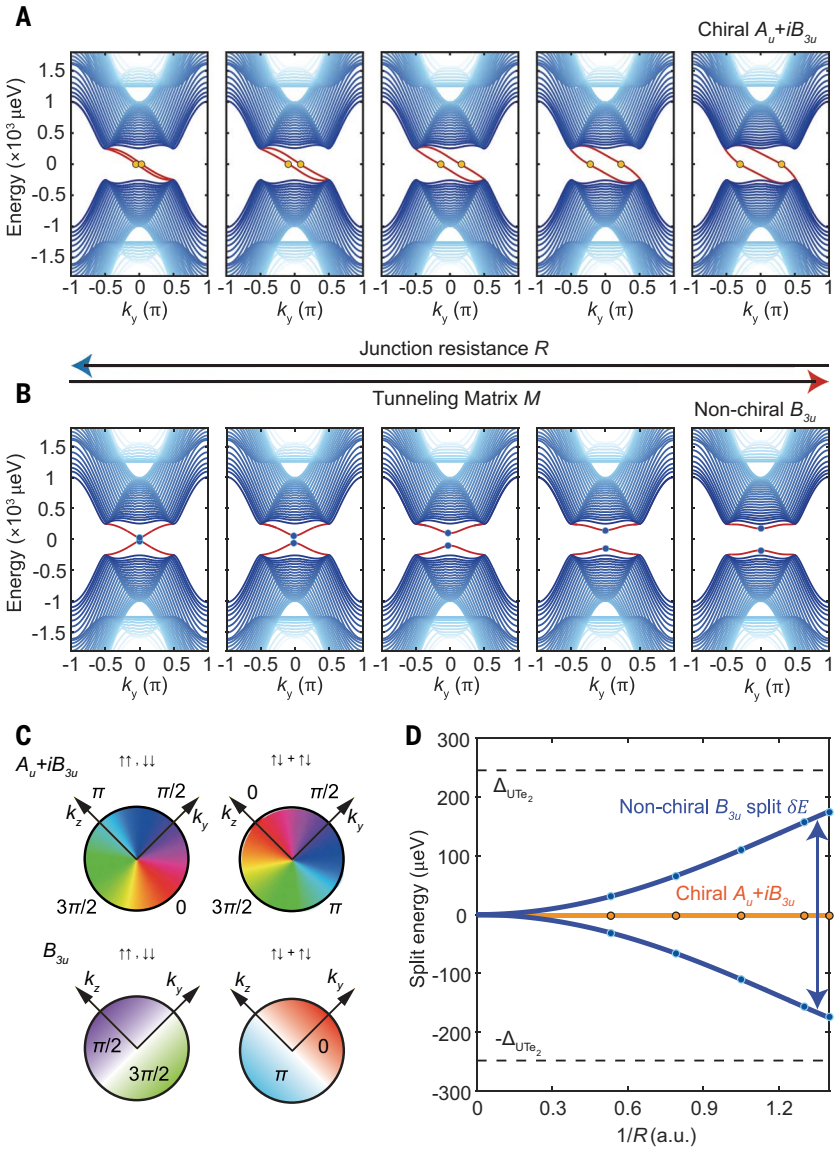

Fig. 3. Order parameter–specific TSB effects with enhanced tunneling. (**A**) Calculated quasiparticle bands within the SIP interface between Nb and UTe_2 with $\delta\phi = \pi/2$ as a function of tunneling matrix element $|M|$. Here the chiral order parameter has $A_u + iB_{3u}$ symmetry. As $|M| \to 0$ and $R \to \infty$, the chiral TSB crosses $E = 0$. With increasing $|M|$ (diminishing R), the effect of the s-wave electrode in the SIP model generates two chiral TSBs inside the UTe_2 superconducting gap for all $E < \Delta_{UTe_2}$, meaning that the zero-energy $dI/dV|_{SIP}$ peak will be virtually unperturbed (the points where the TSB crosses $E = 0$ are indicated by orange circles). (**B**) As in (A), but with a nonchiral TSB that also crosses $E = 0$. With increasing $|M|$ (diminishing R), the effect of the s-wave electrode splits the quasiparticle bands into two (the split is indicated by blue circles), neither of which crosses $E = 0$. This key observation means that the zero-energy $a(0) = dI/dV|_{SIP}$ Andreev conductance peak must split into two particle-hole symmetric maxima separating as $|M|$ is increased. (**C**) Examples of possible order parameter **k**-space phase evolution for UTe_2 as used in (A) and (B). Top panel shows the equatorial ($k_x = 0$) complex phase values of $\Delta_{\mathbf{k}}$ and spin-triplet configurations for chiral order parameter $A_u + iB_{3u}$ (table S2). Bottom panel shows the equatorial ($k_x = 0$) values of $\Delta_{\mathbf{k}}$ and spin-triplet configurations for nonchiral order parameter B_{3u} (table S1). The chiral $A_u + iB_{3u}$ order parameter has a continuous phase winding, in contrast to the discontinuous phase change in the B_{3u} order parameter. (**D**) Calculated energy splitting δE of the zero-energy $a(0) = dI/dV|_{SIP}$ Andreev conductance peak as a function of tunneling matrix element $|M| \sim 1/R$. The δE is zero for $A_u + iB_{3u}$ (orange) at all tunneling matrices $|M|$. However, δE increases as a function of $|M| \sim 1/R$ for a B_{3u} (blue) order parameter, within the SIP model shown in Fig. 2A. The orange circles correspond to the predicted TSB crossing points in (A). The blue circles correspond to the predicted TSB termination points in (B).

parameter with $A_u + iB_{3u}$ symmetry: A chiral TSB spans the full energy range $-\Delta_{UTe_2} \le E \le \Delta_{UTe_2}$, crossing the Fermi level ($E = 0$) and generating a finite density of quasiparticle states $N(|E| < \Delta_{UTe_2})$. Similarly, Fig. 2C shows the quasiparticle spectrum versus k_y at $k_x = 0$ for a nonchiral order parameter with B_{3u} symmetry: two nonchiral TSBs span $-\Delta_{UTe_2} \le E \le \Delta_{UTe_2}$, and feature $E = 0$ states generating a finite $N(|E| < \Delta_{UTe_2})$. Although these TSBs have dispersion in both the positive and negative k_y directions and can backscatter, their gaplessness is protected by time-reversal symmetry with $T^2 = -I$. Hence, solely on the basis of $N(|E| < \Delta_{UTe_2})$ of the TSB, one cannot discriminate between the two symmetries of $\Delta_{\mathbf{k}}$.

Instead, we explored how to distinguish a chiral from a nonchiral $\Delta_{\mathbf{k}}$ by using scanned Andreev tunneling microscopy and spectroscopy. Specifically, within the SIP model, we calculated the Andreev conductance $a(V) = dI/dV|_{SIP}$ between Nb and UTe_2 using the nonchiral TSB and demonstrated that a sharp $a(V)$ peak should occur surrounding zero bias [section 7 of (*9*)]. Because the TSB quasiparticles subtending this peak are protected by time-reversal symmetry and because Andreev reflection of TSB quasiparticles allows efficient transfer of charge $2e$ across the junction, the peak's sharpness is robust. This makes scanned Andreev tunneling spectroscopy an ideal approach for studying superconductive topological surface bands in ITS.

Downloaded from https://www.science.org at University of Maryland College Park on June 16, 2025

Depending on whether UTe_2 is hypothesized as a chiral or nonchiral superconductor, the TSB quasiparticles are themselves chiral (Fig. 2B) or nonchiral (Fig. 2C). As the tunneling matrix element to the s-wave electrode $|M|\rightarrow 0$, these phenomena are indistinguishable, but as $|M|$ increases, the wave functions of Nb overlap those of UTe_2, allowing detection of the TSB quasiparticles at the s-wave electrode. Figure 3A shows the predicted quasiparticle bands within the SIP interface for $A_u + iB_{3u}$ symmetry (Fig. 3C) versus increasing $|M|$ [sections 4 and 5 of (*9*)]. With increasing $|M| \sim 1/R$, where R is the SIP tunnel junction resistance, the proximity effect of the s-wave electrode generates two chiral TSBs for all $|E| < \Delta_{UTe_2}$, both of which cross $E = 0$. Hence, for the chiral $\Delta_{\mathbf{k}}$, the zero-energy $N(E)$ will be virtually unperturbed by increasing $|M|$. Equivalently, Fig. 3B presents the TSB of quasiparticles within the SIP interface as a function of $|M|$ for the nonchiral order parameter with B_{3u} symmetry (Fig. 3C). When $|M|\rightarrow 0$, the nonchiral TSB crosses $E = 0$. But with increasing $|M| \sim 1/R$, time-reversal symmetry breaking due to the s-wave electrode splits the TSB of the quasiparticles into two, neither of which cross $E = 0$. This reveals that the $N(0)$ peak must split as the zero-energy quasiparticles of the TSB disappear, generating two particle-hole symmetric $N(E)$ maxima at finite energy. The pivotal concept is thus: Whereas the chiral TSB in Fig. 2B requires no symmetry to protect it, the nonchiral TSB of

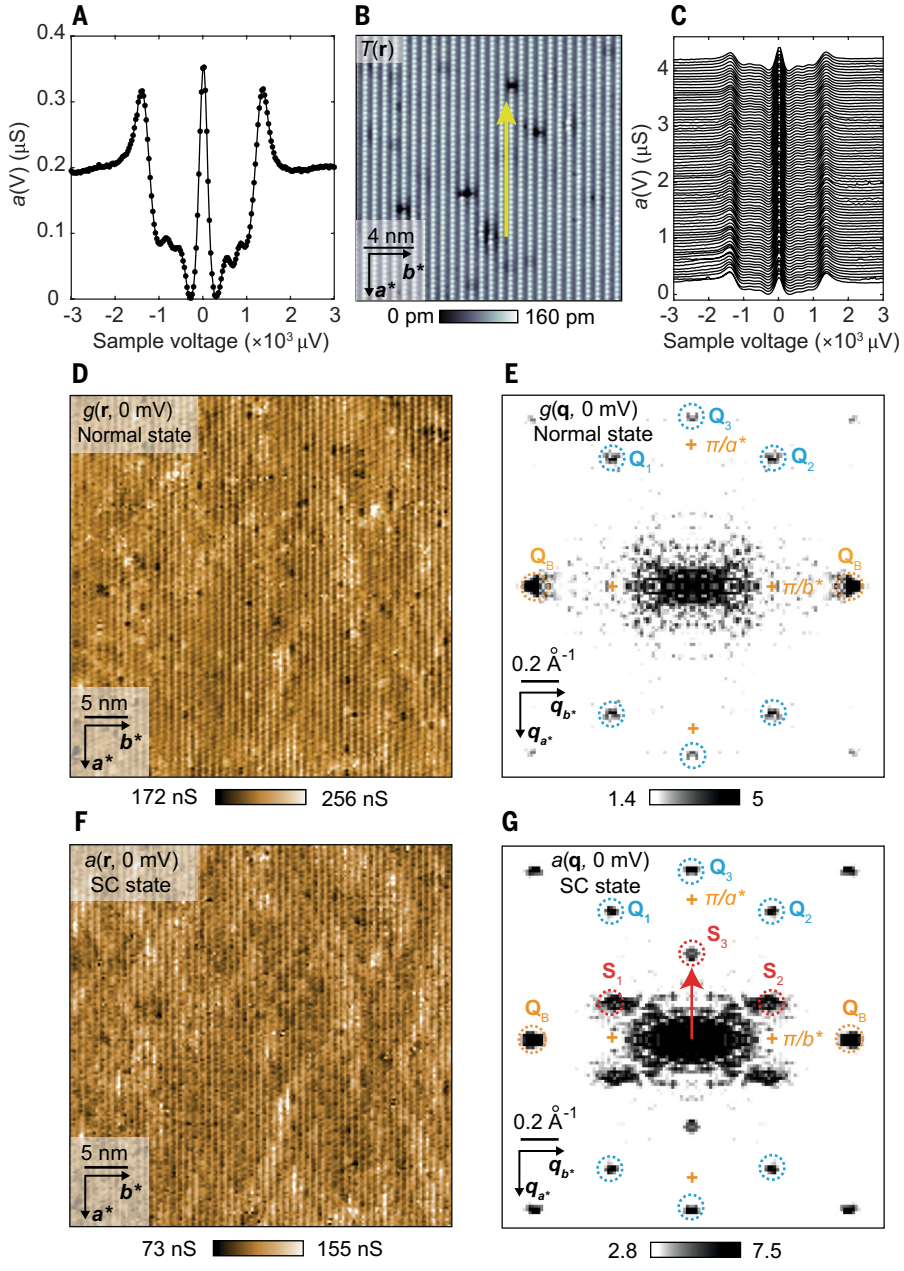

Fig. 4. Discovery of Andreev conductance spectrum *a*(*V*) for Nb/UTe_2 tunneling. (**A**) Typical SIP Andreev conductance spectrum $a(V) \equiv dI/dV|_{SIP}$ measured with a Nb scan tip on UTe_2 (0-11) surface for junction resistance $R = 6$ megohms and $T = 280$ mK. A high-intensity zero-bias $dI/dV|_{SIP}$ peak is detected. (**B**) Typical topographic image $T(\mathbf{r})$ of (0-11) surface ($I_s = 0.2$ nA, $V_s = 5$ mV). (**C**) Evolution of measured $a(\mathbf{r}, V)$ across the (0-11) surface of UTe_2 indicated by the yellow arrow in (B) for junction resistance $R = 6$ megohms and $T = 280$ mK. The zero-bias $dI/dV|_{SIP}$ peaks are universal and robust, indicating that the zero-energy ABS is omnipresent. (**D**) Measured $g(\mathbf{r}, 0)$ at $T = 4.2$ K in the normal state of UTe_2. (**E**) Measured $g(\mathbf{q}, 0)$ is the Fourier transform of $g(\mathbf{r}, 0)$ in (D). (**F**) Superconductive tip–measured $a(\mathbf{r}, 0)$ at $T = 280$ mK in the UTe_2 superconducting state. This image introduces visualization of the spatial configurations of a zero-energy TSB at the surface of UTe_2. (**G**) Superconductive tip–measured $a(\mathbf{q}, 0)$ at $T = 280$ mK in UTe_2: the Fourier transform of $a(\mathbf{r}, 0)$ in (F). Three specific new incommensurate scattering wave vectors, $\mathbf{S}_1$, $\mathbf{S}_2$, and $\mathbf{S}_3$, are indicated by red circles.

Downloaded from https://www.science.org at University of Maryland College Park on June 16, 2025

Fig. 2C will open a gap if time-reversal symmetry is broken. This occurs because the SIP model for a nonchiral $\Delta_{\mathbf{k}}$ (Fig. 2C) predicts strong $|M|$ locking of the relative phase $\delta\phi$ between the two superconductors at $\delta\phi = \pi/2$ to minimize the total energy of the SIP junction [sections 4 and 5 of (*9*)], thus breaking time-reversal symmetry. Conversely, the value of $\delta\phi$ is irrelevant for a chiral $\Delta_{\mathbf{k}}$ (Fig. 2B) because the TSB at the interface remains gapless for any $\delta\phi$ (i.e., the chiral TSB requires no symmetry to protect it). Figure 3D shows the quantitatively predicted splitting of $N(0)$ into two particle-hole symmetric $N(E)$ maxima as a function of $|M|$ for a chiral $\Delta_{\mathbf{k}}$ (orange) and for a nonchiral $\Delta_{\mathbf{k}}$ (blue), within the SIP model of Fig. 2A [sections 4 and 5 of (*9*)]. The decisive fact revealed by this SIP model for Andreev tunneling between an s-wave electrode and a p-wave topological superconductor through the latter's TSB, is that a nonchiral pairing state can be clearly distinguished from a chiral pairing state.

Zero-energy Andreev conductance peak in UTe_2

To search for such phenomena, UTe_2 samples were introduced to a superconductive-tip (*38*–*43*) scanning tunneling microscope, cleaved at 4.2 K in cryogenic ultrahigh vacuum, inserted to the scan head, and cooled to $T = 280$ mK. A typical topographic image $T(\mathbf{r})$ of the (0-11) cleave surface as measured by a superconductive Nb tip is shown in section 8 of (*9*) with atomic periodicities defined by vectors $\mathbf{a}^*$, $\mathbf{b}^*$, where $\mathbf{a}^* = \mathbf{a} = 4.16$ Å is the $\hat{x}$-axis unit-cell vector and $\mathbf{b}^* = 7.62$ Å is a vector in the $\hat{y}$:$\hat{z}$ plane. As the temperature is reduced, several peaks appear within the overall energy gap; these are clear characteristics of the UTe_2 surface states because when the tip is traversed across an adsorbed (non-UTe_2) metal cluster, the subgap peaks disappear [section 8 of (*9*)]. Most notably, for Nb scan tips on the atomically homogeneous (0-11) UTe_2 surface, a sharp zero-energy peak appears in the spectrum as shown in Fig. 4A. This robust zero-bias $dI/dV|_{SIP}$ peak is observed universally, as exemplified, for example, by Fig. 4, B and C. These phenomena are not due to Josephson tunneling, because the zero-bias conductance $a(0)$ of Nb/UTe_2 is orders of magnitude larger than it could possibly be owing to Josephson currents through the same junction, and because $a(0)$ grows linearly with falling R before diminishing steeply as R is further reduced, whereas $g(0)$, because of Josephson currents, should grow continuously as $1/R^2$ [section 8 of (*9*)]. Moreover, the SIP model predicts quantitatively that such an intense $a(0)$ peak should occur if UTe_2 $\Delta_{\mathbf{k}}$ supports a TSB within the interface (Fig. 2A) and because Andreev transport, owing to its quasiparticles, allows zero-bias conductance to the Nb electrode [Fig. 2D and section 7 of (*9*)].

This discovery provides an excellent opportunity to explore the TSB quasiparticles of a nodal odd-parity superconductor. To do so, we focused on a 44 nm by 44 nm field of view (FOV) and, for comparison, first imaged conventional differential conductance at zero-bias $g(\mathbf{r}, 0)$ at $T = 4.2$ K in the normal state of UTe_2 as shown in Fig. 4D. The normal-state QPI signature $g(\mathbf{q}, 0)$ shown in Fig. 4E, is found from Fourier transform of $g(\mathbf{r}, 0)$ in Fig. 4D. Next, Andreev differential conductance $a(\mathbf{r}, V) \equiv dI/dV|_{SIP}(\mathbf{r}, V)$ measurements using a superconductive Nb tip were carried out in the identical FOV at $T = 280$ mK, deep in the UTe_2 superconducting state [Fig. 4F and section 10 of (*9*)]. Note that $a(\mathbf{r}, V)$ represents a two-electron process and is thus not simply proportional to the density of TSB quasiparticle states $N(\mathbf{r}, E)$ but, instead, to the Andreev conductance. Our $a(\mathbf{r}, 0)$ imaging was then carried out in bias-voltage range $V = 0 \pm 150$ μV inside the $dI/dV|_{SIP}$ peak (Fig. 4A). Such images introduce atomic-scale visualization of zero-energy quasiparticles of a superconductive TSB. The Andreev QPI signature $a(\mathbf{q}, 0)$ of these zero-energy quasiparticles is shown in Fig. 4G. Here, three new scattering wave vectors—$\mathbf{S}_1$, $\mathbf{S}_2$, and $\mathbf{S}_3$—are indicated by red circles. Because $\mathbf{S}_3$ exists only in the superconducting state and only for $|E| \lesssim 150$ μeV, it cannot be attributed to any new charge-ordered state [section 10 of (*9*)] but is generated by TSB quasiparticles. And,

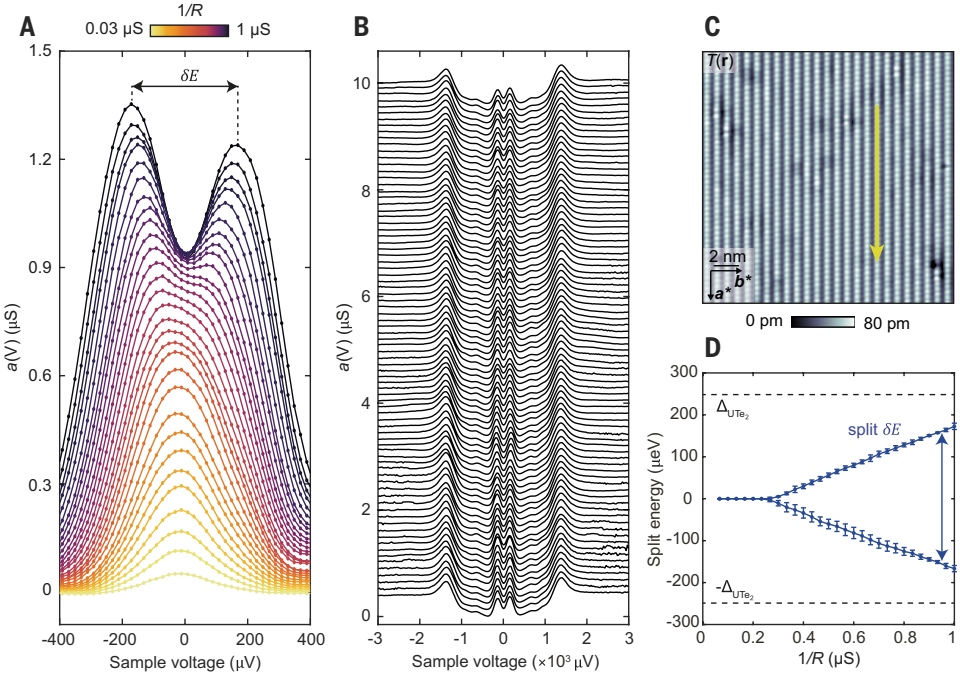

Fig. 5. Evolution and splitting of *a*(*V*) peak with enhanced s-wave hybridization. (**A**) Measured evolution of $a(V) \equiv dI/dV|_{SIP}$ at $T = 280$ mK in UTe_2 as a function of decreasing junction resistance R (i.e., decreasing the tip-sample distance) and thus increasing tunneling matrix element $|M| \sim 1/R$. The $a(V)$ spectra start to split when the junction resistance falls below $R \sim 5$ megohms. (**B**) Evolution of measured $a(\mathbf{r}, V)$ splitting across the (0-11) surface of UTe_2 along the yellow arrow indicated in (C), at junction resistance $R = 3$ megohms and $T = 280$ mK, demonstrating that $a(\mathbf{r}, V)$ split peaks are pervasive at low junction resistance R and high tunneling matrix $|M|$. (**C**) Topographic image $T(\mathbf{r})$ of (0-11) surface ($I_s = 0.2$ nA, $V_s = 3$ mV, $T = 280$ mK) showing the trajectory of the $a(\mathbf{r}, V)$ spectra that demonstrate the universality of $a(V)$ splitting in (B). (**D**) Measured energy splitting of $a(V)$ at $T = 280$ mK in UTe_2 versus $1/R$. These data may be compared with predictions of $a(V)$ splitting within the SIP model for $A_u + iB_{3u}$ and B_{3u} order parameters of UTe_2 (Fig. 3D).

Downloaded from https://www.science.org at University of Maryland College Park on June 16, 2025

because a closed Fermi surface has been hypothesized for UTe_2 from both angle-resolved photoemission and quantum oscillation research (*44*–*46*), $\mathbf{S}_3$ is not inconsistent with an *a*-axis internodal scattering wave vector on such a Fermi surface.

Nature of the UTe_2 superconductive order parameter $\Delta_{\mathbf{k}}$

Finally, to determine spectroscopically whether the UTe_2 order parameter is chiral, we measured the evolution of Andreev conductance $a(V)$ at $T = 280$ mK as a function of decreasing junction resistance R or equivalently increasing tunneling matrix element $|M|$. Figure 5A shows clearly the strong energy splitting δE observable in $a(V)$, which first appears and then evolves with increasing $1/R$. Figure 5B shows the measured $a(\mathbf{r}, V)$ splitting across the (0-11) surface of UTe_2 along the yellow arrow indicated in Fig. 5C for $R = 3$ megohms, demonstrating that $a(\mathbf{r}, V)$ split peaks are pervasive. Decisively, from measurements in Fig. 5A, we plotted in Fig. 5D the measured δE between peaks in $a(\mathbf{r}, V)$ at $T = 280$ mK versus $1/R$. On the basis of predictions for energy splitting δE within the SIP model presented in Fig. 3D for chiral $\Delta_{\mathbf{k}}$ (Fig. 3A) and nonchiral $\Delta_{\mathbf{k}}$ (Fig. 3B), a chiral $\Delta_{\mathbf{k}}$ appears to be ruled out. However, here we note that the SIP model assumes a planar junction with translational invariance parallel to the interface: This implies mirror symmetry ($k_x \rightarrow -k_x$), which the STM tip could break, compromising the protection of the nonchiral state and splitting a zero-bias peak [section 6 of (*9*)]. Nonetheless, as a chiral TSB is symmetry independent, our conclusion holds: Splitting of the zero-bias Andreev conductance peak indicates nonchiral pairing in UTe_2.

Thus, the chiral order parameters $A_u + iB_{1u}$ and $B_{3u} + iB_{2u}$ proposed for UTe_2 seem inapplicable because of the observed Andreev conductance $a(0)$ splitting (Fig. 5A). Within the four possible odd-parity time-reversal–preserving symmetries, A_u, B_{1u}, B_{2u}, and B_{3u}, the isotropic A_u order parameter appears insupportable because its TSB is a Majorana cone of Bogoliubons with zero density of states at zero energy (*7*), meaning that Andreev conductance $a(0)$ would be highly suppressed. Among the remaining three possible order parameters, B_{1u}, B_{2u}, and B_{3u}, all should exhibit the Andreev conductance $a(0)$ splitting that is observed. However, if the $\mathbf{S}_3$ modulations are due to *a*-axis internodal scattering, then the B_{3u} state is favored because its nodes occur along the *a* axis.

Discussion and outlook

Modeling Andreev conductance from an s-wave superconductor through the intervening TSB of an intrinsic topological superconductor reveals a zero-energy Andreev conductance maximum at surfaces parallel to the nodal axis. Further, splitting of this Andreev conductance peak owing to proximity of an s-wave superconductor signifies a 3D ITS, with $\Delta_{\mathbf{k}}$ preserving time-reversal symmetry. Although the B_{1u}, B_{2u}, or B_{3u} states could all be consistent with such a phenomenology, should the $a(\mathbf{r}, 0)$ modulations at wave vector $\mathbf{S}_3$ result from *a* axis–oriented energy-gap nodes, then the complete experimental data imply that $\Delta_{\mathbf{k}}$ of UTe_2 is in the B_{3u} state. Future experiments using energy-resolved quasiparticle interference imaging of the TSB may explore this premise even more directly. Most generally, use of SIP Andreev conductance spectroscopy for quasiparticle surface band detection and $\Delta_{\mathbf{k}}$ symmetry determination opens new avenues for discovery and exploration of 3D intrinsic topological superconductors.

REFERENCES AND NOTES

1. M. R. Norman, *Science* **332**, 196–200 (2011).
2. P. W. Anderson, P. Morel, *Phys. Rev.* **123**, 1911–1934 (1961).
3. R. Balian, N. R. Werthamer, *Phys. Rev.* **131**, 1553–1564 (1963).
4. D. Vollhardt, P. Woelfle, *The Superfluid Phases of Helium 3* (Taylor & Francis, 1990).
5. A. J. Leggett, *Quantum Liquids: Bose Condensation and Cooper Pairing in Condensed-Matter Systems* (Oxford Univ. Press, 2006).
6. A. P. Schnyder, S. Ryu, A. Furusaki, A. W. W. Ludwig, *Phys. Rev. B* **78**, 195125 (2008).
7. A. P. Schnyder, P. M. R. Brydon, *J. Phys. Condens. Matter* **27**, 243201 (2015).
8. C. Kallin, J. Berlinsky, *Rep. Prog. Phys.* **79**, 054502 (2016).
9. Supplementary materials.
10. D. Aoki *et al.*, *J. Phys. Soc. Jpn.* **88**, 043702 (2019).
11. S. Ran *et al.*, *Science* **365**, 684–687 (2019).
12. D. Aoki *et al.*, *J. Phys. Condens. Matter* **34**, 243002 (2022).
13. P. F. S. Rosa *et al.*, *Commun. Mater.* **3**, 33 (2022).
14. Y. Tokunaga *et al.*, *J. Phys. Soc. Jpn.* **88**, 073701 (2019).
15. G. Nakamine *et al.*, *J. Phys. Soc. Jpn.* **88**, 113703 (2019).
16. H. Sakai *et al.*, *Phys. Rev. Mater.* **6**, 073401 (2022).
17. H. Matsumara *et al.*, *J. Phys. Soc. Jpn.* **92**, 063701 (2023).
18. H. Fujibayashi *et al.*, *J. Phys. Soc. Jpn.* **91**, 043705 (2022).
19. T. Metz *et al.*, *Phys. Rev. B* **100**, 220504(R) (2019).
20. S. Suetsugu *et al.*, *Sci. Adv.* **10**, eadk3772 (2024).
21. S. Kittaka *et al.*, *Phys. Rev. Res.* **2**, 032014(R) (2020).
22. I. M. Hayes *et al.*, *Science* **373**, 797–801 (2021).
23. L. P. Cairns, C. R. Stevens, C. D. O'Neill, A. Huxley, *J. Phys. Condens. Matter* **32**, 415602 (2020).
24. Y. Iguchi *et al.*, *Phys. Rev. Lett.* **130**, 196003 (2023).
25. K. Ishihara *et al.*, *Nat. Commun.* **14**, 2966 (2023).
26. L. Jiao *et al.*, *Nature* **579**, 523–527 (2020).
27. M. O. Ajeesh *et al.*, *Phys. Rev. X* **13**, 041019 (2023).
28. J. E. Hoffman *et al.*, *Science* **297**, 1148–1151 (2002).
29. T. Hanaguri *et al.*, *Physica C* **460**, 954–955 (2007).
30. M. P. Allan *et al.*, *Nat. Phys.* **9**, 468–473 (2013).
31. M. P. Allan *et al.*, *Science* **336**, 563–567 (2012).
32. P. O. Sprau *et al.*, *Science* **357**, 75–80 (2017).
33. R. Sharma *et al.*, *Proc. Natl. Acad. Sci. U.S.A.* **117**, 5222–5227 (2020).
34. Q. Gu *et al.*, *Nature* **618**, 921–927 (2023).
35. A. Aishwarya *et al.*, *Nature* **618**, 928–933 (2023).
36. S. Bae *et al.*, *Nat. Commun.* **12**, 2644 (2021).
37. Q. H. Wang, D. H. Lee, *Phys. Rev. B* **67**, 020511(R) (2003).
38. M. H. Hamidian *et al.*, *Nature* **532**, 343–347 (2016).
39. D. Cho, K. M. Bastiaans, D. Chatzopoulos, G. D. Gu, M. P. Allan, *Nature* **571**, 541–545 (2019).
40. X. Liu, Y. X. Chong, R. Sharma, J. C. Davis, *Science* **372**, 1447–1452 (2021).
41. X. Liu, Y. X. Chong, R. Sharma, J. C. S. Davis, *Nat. Mater.* **20**, 1480–1484 (2021).
42. S. M. O'Mahony *et al.*, *Proc. Natl. Acad. Sci. U.S.A.* **119**, e2207449119 (2022).
43. W. Chen *et al.*, *Proc. Natl. Acad. Sci. U.S.A.* **119**, e2206481119 (2022).
44. S. Fujimori *et al.*, *J. Phys. Soc. Jpn.* **88**, 103701 (2019).
45. L. Miao *et al.*, *Phys. Rev. Lett.* **124**, 076401 (2020).
46. C. Broyles *et al.*, *Phys. Rev. Lett.* **131**, 036501 (2023).
47. Q. Gu, Pair Wave Function Symmetry in UTe_2 from Zero-Energy Surface State Visualization [Data set], version 2, Zenodo (2025); https://doi.org/10.5281/zenodo.15021425.

ACKNOWLEDGMENTS

We acknowledge and thank M. Aprili, C. Bena, J. E. Hoffman, E.-A. Kim, S. Kivelson, A. P. Mackenzie, V. Madhavan, and C. Pepin for key discussions and guidance. **Funding:** Research at the University of Maryland was supported by the US Department of Energy award DE-SC-0019154 (sample characterization), the Gordon and Betty Moore Foundation's EPiQS Initiative through grant GBMF9071 (materials synthesis), NIST, and the Maryland Quantum Materials Center. Research at Washington University in St. Louis was supported by National Science Foundation (NSF) Division of Materials Research award DMR-2236528. S.W. and J.C.S.D. acknowledge support from the European Research Council (ERC) under award DLV-788932. X.L. acknowledges support from the Department of Energy (DE-SC0025021). Q.G., S.W., J.P.C., and J.C.S.D. acknowledge support from the Moore Foundation's EPiQS Initiative through grant GBMF9457. J.C.S.D. acknowledges support from the Royal Society under award R64897. J.P.C., K.Z., and J.C.S.D. acknowledge support from Science Foundation Ireland under award SFI 17/RP/5445. D.-H.L. was supported by the US Department of Energy, Office of Science, Basic Energy Sciences, Materials Sciences and Engineering Division, contract DE-AC02-05-CH11231, within the Quantum Materials Program (KC2202). **Author contributions:** D.-H.L. and J.C.S.D. conceived of and supervised the project. S.R., C.B., S.S., J.A.H., N.P.B., and J.P. developed, synthesized, and characterized materials; D.-H.L. provided the theoretical motivation and the SIP model; Q.G., S.W., J.P.C., K.Z., and X.L. carried out the experiments; Q.G., S.W., K.Z., and J.P.C. developed and implemented the analysis. J.C.S.D. and D.-H.L. wrote the paper, with key contributions from S.W., Q.G., K.Z., J.P.C., and X.L. The paper reflects contributions and ideas of all authors. Conceptualization: J.C.S.D., D.-H.L., Q.G.; Methodology: J.C.S.D., D.-H.L., Q.G.; Materials: S.R., C.B., S.S., J.A.H., N.P.B., J.P.; Investigation: Q.G., S.W., J.P.C., K.Z.; Visualization: Q.G., S.W., J.P.C., K.Z.; Funding acquisition: J.C.S.D., J.P., D.H.L.; Project administration: J.C.S.D.; Supervision: J.C.S.D., D.H.L.; Writing – original draft: J.C.S.D., D.-H.L.; Writing – review & editing: J.C.S.D., D.-H.L., S.W., K.Z., J.P.C., X.L., Q.G. **Competing interests:** The authors declare that they have no competing interests. **Data and materials availability:** All data are available in the main text, the supplementary materials, and in Zenodo (*47*).

License information: Copyright © 2025 the authors, some rights reserved; exclusive licensee American Association for the Advancement of Science. No claim to original US government works. https://www.science.org/about/science-licenses-journal-article-reuse

SUPPLEMENTARY MATERIALS

science.org/doi/10.1126/science.adk7219
Materials and Methods; Supplementary Text; Figs. S1 to S8; Tables S1 and S2; References (*48*–*54*)

Submitted 15 September 2023; resubmitted 1 February 2024; accepted 2 April 2025

10.1126/science.adk7219

Downloaded from https://www.science.org at University of Maryland College Park on June 16, 2025